Crossed-Beam Energy Transfer in Direct-Drive Implosions

Introduction

The direct-drive approach to inertial confinement fusion (ICF)[1,2] is based on the implosion, compression, and subsequent ignition of millimeter-diameter cryogenic deuterium–tritium (DT) ice shell targets using high-intensity ($I \sim 10^{14}$ to 10^{15} W/cm^2) laser irradiation [Fig. 129.1(a)]. Direct drive offers the possibility of higher gain than from indirect-drive implosions of the same laser energy.[4] [Reference 3 is cited in the caption of Fig. 129.1(a) below.] To validate physics effects in direct-drive–ignition experiments planned for the National Ignition Facility (NIF),[5] the experiments are carried out on the OMEGA Laser System,[6] which employs 60 laser beams with a total energy of up to 30 kJ [Figs. 129.1(b) and 129.1(c)]. Experiments to study ignition-relevant conditions require a laser energy of ~1 MJ and will be conducted on the NIF in the polar-drive configuration.[7]

High-intensity incident light is absorbed in the corona of direct-drive targets, and the released heat drives the implosions by ablating the outer target surface. The dominant absorption mechanism on the OMEGA and NIF lasers, which operate on a wavelength λ_L = 351 nm, is inverse bremsstrahlung, or "collisional absorption."[8] Laser light is absorbed in a relatively narrow radial region with electron densities n_e from ~0.5 to 1 n_{cr}, where $n_{cr} = \pi c^2 m_e \big/ \lambda_L^2 e^2$ is the critical density, m_e is the electron mass, e is the electron charge, and c is the speed of light. The symmetric illumination of targets with many laser beams, crossing each other at different angles and directions, creates conditions for transferring energy among beams because of electromagnetically seeded, low-gain stimulated Brillouin scattering (SBS).[9] Figure 129.2 illustrates the geometry of crossing rays when the most-efficient energy transfer occurs at the radii outside the highest-absorption region with n_e from ~0.1 to 0.5 n_{cr}. The outgoing edge-beam light in Beam 1 seeds perturbations to the incoming center-beam light in Beam 2 (Fig. 129.2), scattering this light outward. Because of this scattering, the incoming light fails to penetrate into the most-absorbing region of the corona (where $n_e \sim n_{cr}$) and
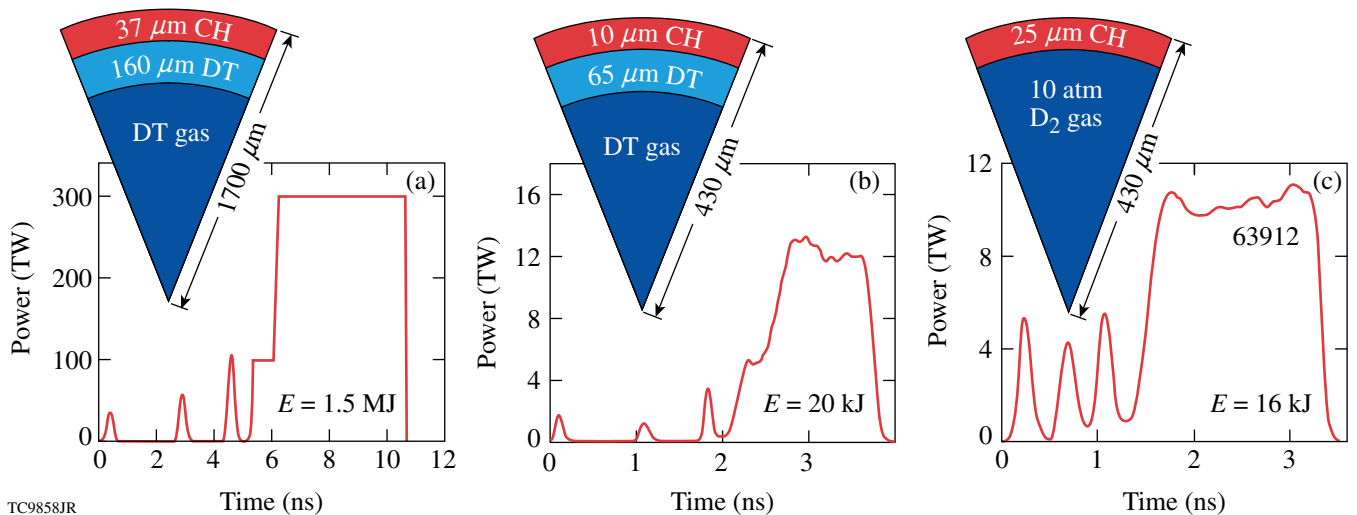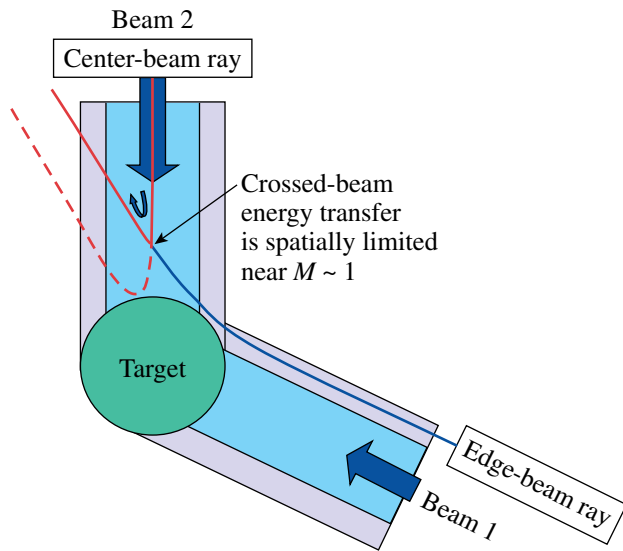

Figure 129.1
(a) A 1.5-MJ direct-drive NIF ignition design.[3] This design utilizes a triple-picket pulse and obtains an energy gain of about 50. (b) Typical cryogenic OMEGA target. This target is a scaled-down version of the design in (a) and is optimized for a laser energy of up to 25 kJ. (c) Example of a warm OMEGA target (shot 63912). Such targets are a less-expensive alternative to cryogenic OMEGA targets. The warm targets are used to study laser coupling, hydrodynamic stability, hot-spot formation, and other aspects of implosion physics.
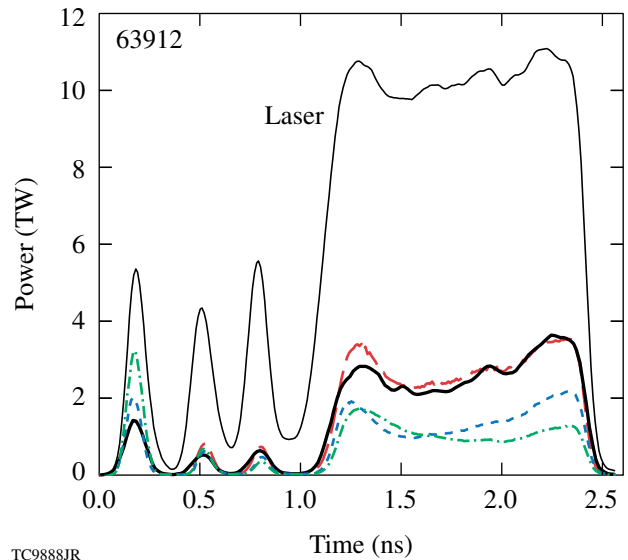
Figure 129.2

Schematic illustration of a laser-ray geometry with the most energetically efficient crossed-beam energy transfer (CBET) in the corona of an implosion target. An incident edge-beam ray (shown in blue) in Beam 1 is refracted and turned outward above the critical radius. On its outgoing trajectory, this ray seeds perturbations to an incoming center-beam ray (shown in red) in Beam 2 that results in energy transfer from the latter ray to the outgoing ray (also shown in red). The energy transfer occurs near the Mach 1 radius, which is typically located at n_e from 0.2 to 0.3 n_{cr}. As the result of CBET, center-beam rays deliver less energy to the maximum absorption region near the critical radius.

Figure 129.3

Reflected light power history measured (thick black line) and simulated using flux-limited transport (green dashed–dotted line), nonlocal transport (blue dashed line), and nonlocal transport with CBET (red dashed line). The thin black line shows the incident laser power. Note good agreement between the measured power history and the simulated one with CBET.

deposits its energy there, as it does without scattering, reducing laser coupling. Calculations show that crossed-beam energy transfer (CBET) becomes important in OMEGA implosions at intensities $I > 10^{14}$ W/cm^2.

Figure 129.3 illustrates the discrepancy between the modeled scattered-light power without CBET in a plastic-shell (CH) implosion driven at $I = 4.5 \times 10^{14}$ W/cm^2 and experimental observations. The green dashed–dotted and blue dashed lines in Fig. 129.3 show simulated powers using flux-limited (with the flux-limiter parameter $f = 0.06$)[10] and nonlocal[11] heat transport models, respectively. These simulations significantly underestimate and are not able to correctly reproduce the measured power[12] shown by the thick solid black line in Fig. 129.3. The simulations overpredict the measured absorption by about 10%. Simulations of the same implosion but including CBET accurately reproduce the measurements (compare red dashed and solid black lines in Fig. 129.3). Simulations including CBET show good agreement with all observables in implosion experiments using different laser energies, pulse shapes, and targets. Examples of these simulations are discussed in Ref. 13

with more examples discussed below. Good agreement with measurements is obtained only in simulations using CBET and nonlocal transport. Simulations using flux-limited transport with or without CBET fail to consistently reproduce experiments.

The performance of implosions can be improved by mitigating CBET.[13] This article considers three mitigation techniques: One technique uses a laser-beam (or focal-spot) diameter smaller than the target diameter. This can be very efficient in reducing CBET and increasing laser coupling, but on the downside the narrow beams introduce beam-overlap nonuniformities, which can degrade the implosion performance. Experiments on OMEGA have been performed to investigate the optimum beam diameters by balancing CBET with the effects of nonuniformity in low-adiabat implosions. This is discussed below in detail. The second technique employs multicolored laser light, which modifies resonance coupling between beams. Using, for example, a two-color split, CBET can be reduced by a factor of 1/2 for the wavelength separation $\Delta\lambda > 5$ Å of the two wavelengths (for 351-nm light). The third technique uses targets with plastic ablators doped with high-Z elements (e.g., Ge).

The following sections describe the simulation technique for modeling CBET (with details described in Appendices A,

B, and C); discuss CBET in OMEGA implosions, comparing simulations and measurements; and consider the three techniques for mitigating CBET: narrow beams, multicolored lasers, and Ge-doped plastic ablators. The conclusions are presented in the final section.

Modeling CBET

The numerical algorithm for CBET considers pairwise interactions of pump light rays (denoted with index j) with probe light rays (denoted with index i). All possible crossings of the pump rays with the probe light on the path ℓ in a target corona are taken into account. The path ℓ is calculated using Snell's law. The intensity of the probe light along ℓ obeys the equation

$$\frac{dI_i}{d\ell} = \xi I_i \sum_j L_{ij}^{-1}, \tag{1}$$

where L_{ij} is the SBS gain length for the rays i and j and ξ is a limiting parameter,[13] $0 < \xi \le 1$ (see the next section). The spatial gain L_{ij} is estimated in the strong damping limit,[8] which is well satisfied in direct-drive implosions,[14] and given in Appendices A and B for the fluid [Eq. (A2)] and kinetic [Eq. (B8)] models, respectively. A random polarization of the illuminating beams in implosions is accounted for in Eq. (1) by increasing L_{ij} by a factor of 2.

The algorithm uses a simplified assumption of spherical symmetry for both the implosion hydrodynamics and laser illumination. Intensity profiles for laser beams can take an arbitrary shape (e.g., super-Gaussian $n = 4$ in the standard OMEGA setup). The algorithm is incorporated into the laser-absorption package of the one-dimensional (1-D) hydrodynamic code *LILAC*,[15] allowing for a self-consistent calculation of laser deposition with CBET.

Simulations of implosions with $I \gtrsim 4 \times 10^{14}$ W/cm² show that the CBET model overpredicts scattered power, indicating the possible presence of additional mechanisms that increase laser coupling. This discrepancy is resolved by introducing a simple model for clamping the ion-acoustic waves.[16] The clamp model was incorporated in *LILAC* and is discussed in Appendix C.

CBET in OMEGA Implosions

OMEGA implosions are used to validate the accuracy of the CBET model, comparing simulations with observables. Laser coupling is characterized by the time-dependent absorption fraction, inferred from scattered-light measurements and scattered-frequency spectra.[12] The hydrodynamic efficiency of simulated implosions can be constrained by bang time (time of rising of the neutron rate)[17] and shell trajectory measurements (inferred from x-ray self-emission images of implosion targets).[18]

Simulations of implosions at $I \gtrsim 4 \times 10^{14}$ W/cm² indicate that the CBET model overpredicts measured scattered light and, as a result, shows earlier bang times. The agreement with experiments can be improved by reducing CBET in simulations. This is accomplished by clamping ion-acoustic waves with the clamp parameter $(\tilde{n}_e/n_e)_{cl}$ (Appendix C).[16] Simulations using a single clamp value show good agreement for implosions with different pulse shapes and intensities up to $I \approx 6 \times 10^{14}$ W/cm² (for higher intensities, see below). Targets with different ablators, however, require different clamping. For example, it was found that $(\tilde{n}_e/n_e)_{cl} \approx 0.1\%$ fits data for plastic and 10% fits data for glass (SiO₂) ablators. In the previous study,[13] CBET was reduced assuming $\xi < 1$ in Eq. (1). This approach is less universal, however, because it requires different ξ depending on the laser energy, pulse shapes, and targets.

The fluid and kinetic versions of the CBET model (Appendices A and B, respectively) were compared using implosions of plastic- and glass-shell targets. Small differences between the results of these versions were observed. The differences are typically smaller than deviations of simulations from measurements. The majority of simulation results discussed here were obtained using the fluid version, which is less computationally expensive.

Figure 129.3 compares measured and simulated scattered-light powers for a triple-picket, warm plastic-shell implosion with a main pulse intensity $I = 4.5 \times 10^{14}$ W/cm² (OMEGA shot 63912).[19] The simulations employing the fluid CBET model with $(\tilde{n}_e/n_e)_{cl} = 0.1\%$ (red dashed line) accurately reproduce the measured time-dependent scattered power (thick solid line).

Figure 129.4 compares measured [Fig. 129.4(a)] and simulated scattered-light spectra with [Fig. 129.4(b)] and without CBET [Figs. 129.4(c) and 129.4(d)] for the same implosion as in Fig. 129.3. The simulated spectra reproduce all basic features of the measured spectrum: time-dependent frequency shifts during pickets and an initial blue shift and later red shift of scattered light during the main pulse. The details and accuracy of reproduction of the measured spectrum depend, however, on the heat-transport model used and the presence of CBET.[20] The simulations using flux-limited transport [Fig. 129.4(c)] underestimate the blue shifts during the first picket and initial part of the main pulse, indicating that the density and velocity
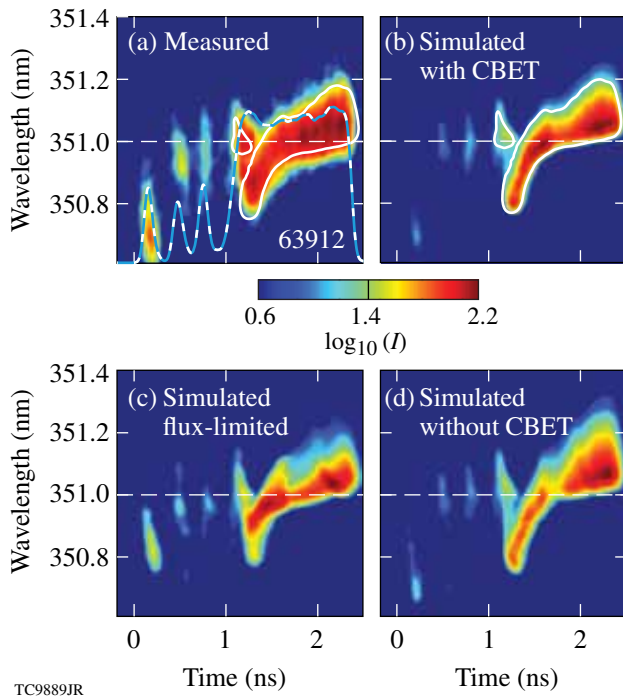
Figure 129.4

(a) Measured and [(b)–(d)] simulated scattered-light spectra for a warm plastic-shell implosion (OMEGA shot 63912). *LILAC* predictions using nonlocal transport and CBET are shown in (b) and simulations without CBET using flux-limited and nonlocal transports are shown in (c) and (d), respectively. The white contours in (a) indicate the shape of the simulated spectrum in (b). The incident light wavelength is represented by the dashed line.
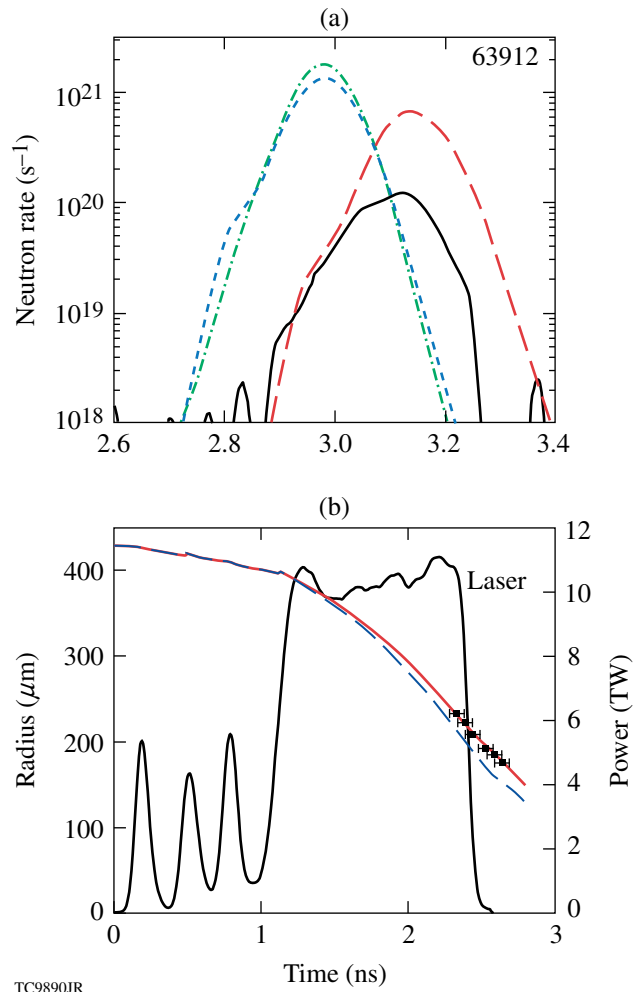

Figure 129.5

(a) Neutron-production history measured (black solid line) and simulated with flux-limited transport (green dashed–dotted line), nonlocal transport (blue dashed line), and nonlocal transport and CBET (red dashed line). The measurements and simulations with CBET show good agreement between bang times, which are estimated as the rise time of the neutron rate. (b) Ablation-front trajectory inferred from x-ray framing camera images[18] (black dots) and the trajectories simulated using nonlocal transport with and without CBET (red solid and blue dashed lines, respectively). The simulations with CBET show good agreement with measurements.

distributions in the target corona are not accurately predicted. The simulations using nonlocal transport without CBET [Fig. 129.4(d)] overestimate the late-time red shift during the main pulse; those with CBET [Fig. 129.4(b)] agree best with the measurements.

The predicted hydrodynamic efficiency of implosions can be verified using measured bang-time and ablation-front trajectories. Figure 129.5(a) shows the measured (solid line) and simulated (blue dashed, green dashed–dotted, and red dashed lines) neutron-production histories for the same implosion as in Fig. 129.3. The experimental bang time for this implosion is about 2.95 ns. The simulations using nonlocal transport and CBET (red dashed line) show bang time coinciding with the measured time within experimental uncertainty. The simulations without CBET, using both flux-limited (green dashed–dotted line) and nonlocal transport (blue dashed line), predict bang times ~200 ps earlier than measured. This is consistent with the higher predicted absorption (or underpredicted scattered-light power) shown in Fig. 129.3.

Figure 129.5(b) shows the measured (squares) and simulated ablation-front trajectories, where the simulations use nonlocal transport with and without CBET (red solid and blue dashed lines, respectively). The trajectory simulated using CBET agrees well with the measured trajectory. The simulations without CBET predict a faster implosion.

Neutron yield is perhaps the most important characteristic of implosions; however, it cannot be directly used to validate the CBET model. This is because the neutron-production

rate strongly depends on temperature and density distributions inside the hot spot.[1] Low-adiabat, warm implosions on OMEGA typically produce yields that are 20% to 25% of *LILAC*-simulated yields. This approximately factor-of-4 yield reduction is unlikely due to inaccuracies in the CBET model and more likely due to asymmetry of implosions. Relative yields, however, are used to study the mitigation of CBET in the **Narrow Beams** section below.

The CBET model was validated using different targets, laser energies, and pulse shapes and shows good and consistent agreement with measurements (see other examples in Ref. 13) up to intensities $I \approx 6 \times 10^{14}$ W/cm^2. At higher intensities of $I \sim 10^{15}$ W/cm^2, the CBET model predicts more scattered light than measured, indicating the presence of an additional absorption mechanism that increases laser coupling. Possible candidates for this mechanism include two-plasmon-decay instability (TPD),[21] which converts incident light into plasma waves with a subsequent dissipation of these waves,[22] and saturation of SBS in intense laser speckles.[23]

Glass-shell implosions were not studied as thoroughly as the plastic-shell implosions discussed above. Only a few implosions were analyzed and were in good agreement with simulations using an appropriate clamp parameter. Figure 129.6 presents an example of a glass-shell implosion that used an 860-μm-diam, 20-μm-thick glass shell filled with 20 atm of D$_2$ gas. A shaped pulse [the thin solid line in Fig. 129.6(a)] with 26 kJ of energy was used to provide an on-target intensity of $I \approx 10^{15}$ W/cm^2.

The best agreement between measured and predicted scattered-light and neutron-production histories [see Figs. 129.6(a) and 129.6(b), respectively] was obtained using simulations with nonlocal transport and CBET, in which $\left(\tilde{n}_e/n_e\right)_{cl} = 10\%$ (compare thick solid and red dashed lines). Simulations without CBET using flux-limited and nonlocal transports [the dashed–dotted and short-dashed lines in Figs. 129.6(a) and 129.6(b)] show significant disagreement with measurements.

Mitigation of CBET

CBET significantly reduces laser coupling in direct-drive implosions. While the laser absorption in a typical OMEGA implosion is reduced by ~10%, the implosion hydrodynamic efficiency is reduced by ~20%. This can be attributed to the laser-deposition area moving outward from the critical surface when CBET is present.[13] Laser coupling can be partially or, in some cases, completely recovered by employing different mitigation techniques for CBET. Three such techniques are considered below. One technique uses narrow laser beams and is extensively tested in OMEGA experiments and simulations. The other two techniques use multicolored lasers and high-Z dopant ablators.

1. Narrow Beams

The idea of using narrow beams to mitigate CBET is illustrated in Fig. 129.2, which shows a ray geometry with the most-efficient energy transfer. By narrowing the beams, one can eliminate edge-beam rays that seed CBET. Figure 129.7 quantitatively illustrates the contribution of different parts of
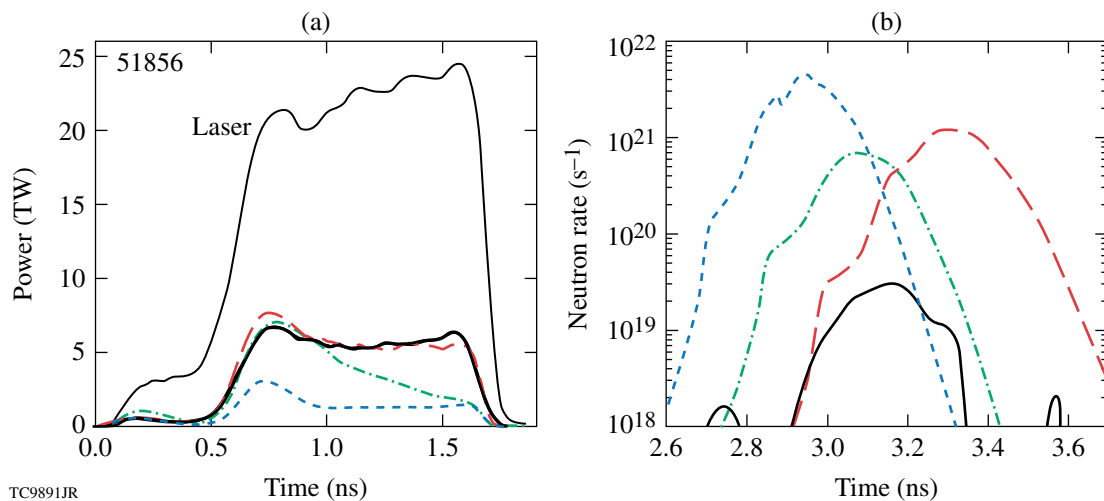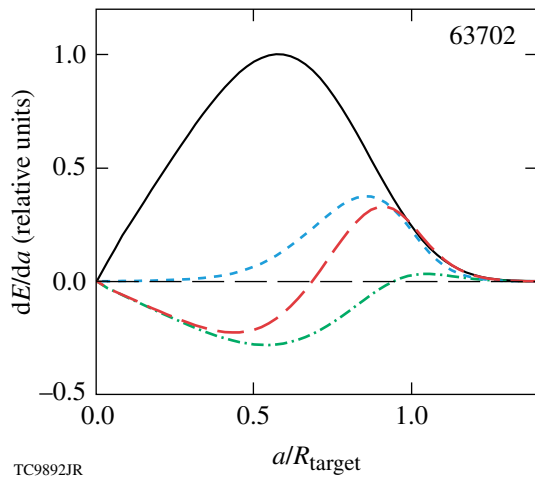

Figure 129.6
(a) Reflected-light power history in a glass-shell implosion (OMEGA shot 51856). (For notations see Fig. 129.3.) (b) Neutron-production history measured and simulated. [For notations see Fig. 129.5(a).] Note good agreement of the measured scattered light and bang time in (a) and (b) with the simulations with CBET and poor agreement with the simulations without CBET.
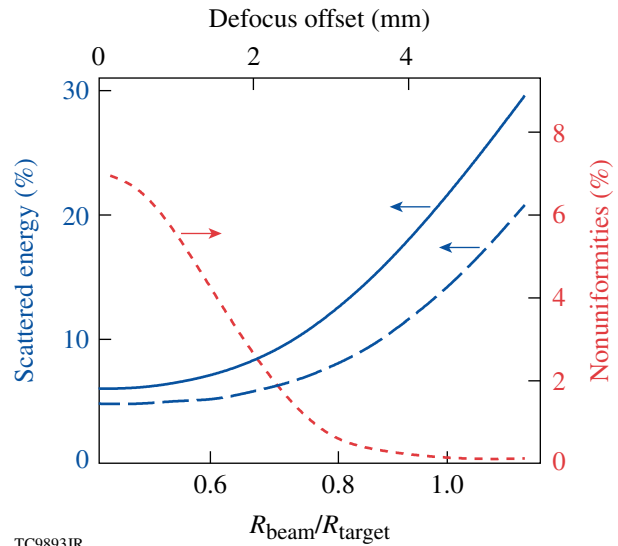
Figure 129.7
Distributions of time-integrated energy transferred between crossing beams as functions of the relative ray impact parameter a/R_{target} in a plastic-shell implosion (OMEGA shot 63702). Distribution of the incident energy is shown by the black solid line. Distribution of the transferred energy for the incoming trajectories is shown by the green dashed–dotted line, for the outgoing trajectories by the blue dashed line, and for whole trajectories (including the incoming and out-going parts) by the red dashed line. The negative dE/da corresponds to energy losses and the positive one to energy gains.

Figure 129.8
Predicted scattered energy and deposition nonuniformities (rms) as functions of R_{beam}/R_{target} in plastic-shell implosions. The scattered energy is normalized to the incident energy. The simulated energies with and without CBET are shown by the blue solid and dashed lines, respectively. The deposition nonuniformities (red dashed line) are calculated using the OMEGA beam-port geometry and time averaging over the whole laser pulse.

beams to CBET. This figure shows the simulated distributions of energy transferred to (when the sign of dE/da is positive) or from (when the sign is negative) light rays with an impact parameter a. The outgoing rays (blue dashed line) always gain energy, and the gain reaches the maximum for rays with a/R_{target} from ~0.7 to 1.1. The incoming rays (green dashed–dotted line) mostly lose energy, transferring it to outgoing rays. This loss takes place for a/R_{target} from 0 to ~0.9 and is peaked at $a/R_{target} \sim 0.5$. The incoming rays with $a/R_{target} \gtrsim 0.9$ gain some energy, but this gain is not significant. The rays with $0.5 \lesssim a/R_{target} \sim 0.9$ lose energy as they travel toward the target and gain it on the way out. The cumulative effect of CBET for the whole ray trajectory (including the incoming and outgoing parts) is shown by the red dashed line in Fig. 129.7. The rays with $a/R_{target} < 0.7$ overall lose energy and the rays with $a/R_{target} > 0.7$ gain energy. This suggests that by eliminating rays with $a/R_{target} > 0.7$, one can completely suppress CBET.

Figure 129.8 shows simulation results for implosions at the same conditions [similar to the one shown in Fig. 129.1(c)] except using different beam radii R_{beam}, which are defined to encircle 95% energy. The beam radius is changed by defocusing beams with an assumed profile $I(r) \sim \exp\left[-(r/r_0)^{2.1}\right]$,

where $r_0 = 135~\mu$m. The ratio R_{beam}/R_{target} is varied from 0.5 to 1.1. The simulations including CBET (solid line) show a decrease in scattered energy when R_{beam}/R_{target} is decreased. The scattered energy in the simulations without CBET (blue dashed line) is reduced as well. This is because smaller beams provide illumination of the target surface by more-normal incident light. Such light penetrates deeper into the target corona and is absorbed more efficiently. Therefore, the benefits of using smaller beams include two aspects: reducing CBET and increasing absorption as a result of more-normal incident light.

The smaller beams can have a negative effect on implosion performance because of increasing beam-overlap nonuniformities. Two-dimensional (2-D) hydrodynamic simulations using the code *DRACO*[24] predict nearly symmetric implosions and small reduction in neutron yield for R_{beam}/R_{target} from ~1 to 0.8 [see Figs. 129.9(a) and 129.9(b)]. Simulations assuming $R_{beam}/R_{target} \lesssim 0.7$ show significantly distorted targets at maximum compression and reduced neutron yields [by a factor of 2 or more, see Fig. 129.9(c)]. These 2-D results agree with the simple calculations of deposition nonuniformities presented in Fig. 129.8 (red dashed line). The calculations predict a significant increase in the nonuniformities in the range of R_{beam}/R_{target} from 0.8 to 0.7. Therefore, these results suggest
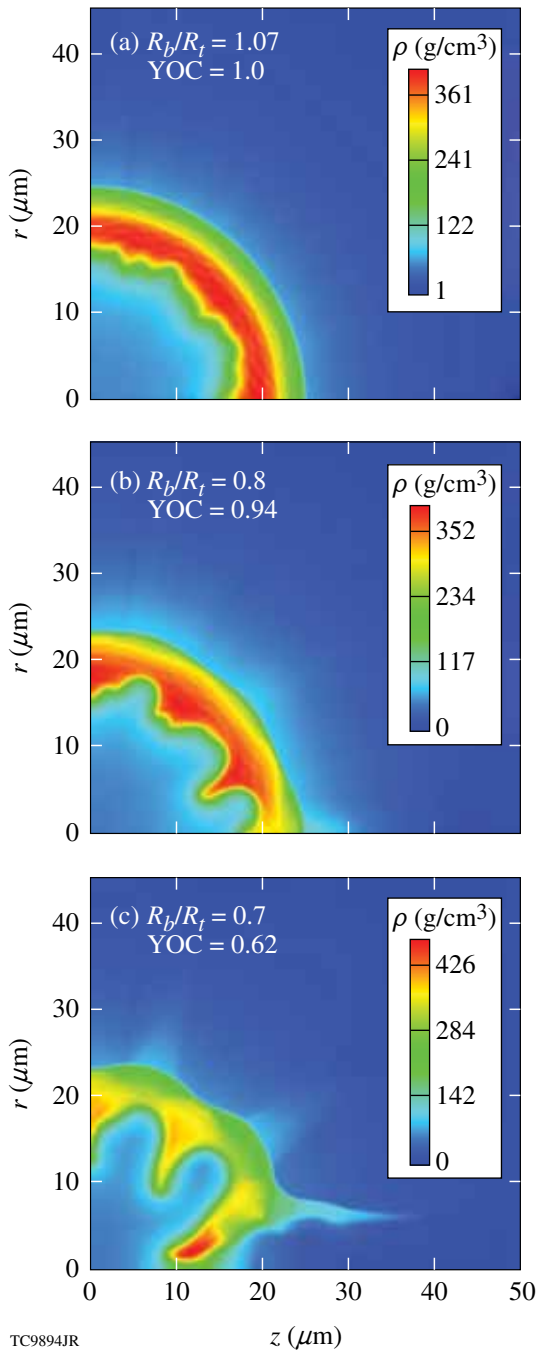
Figure 129.9
Density distributions at maximum compression from 2-D hydrodynamic simulations of implosion targets illuminated by different-sized laser beams: (a) $R_{\text{beam}}/R_{\text{target}} = 1.07$, (b) 0.8, and (c) 0.7. Beam-overlap nonuniformities in the case of small $R_{\text{beam}}/R_{\text{target}}$ result in asymmetric implosions and degradation of neutron yield. Each simulation shows yield over clean (YOC, which is the 2-D yield normalized to the 1-D yield).

an optimum $R_{\text{beam}}/R_{\text{target}} \sim 0.8$ that balances the reduction of CBET and increase of beam-overlap nonuniformities.

Two sets of implosion experiments on OMEGA were performed to investigate the effects of narrow beams. These experiments used triple-picket pulses with a peak overlap intensity $I \approx 4.5 \times 10^{14}$ W/cm^2 that drive targets with an adiabat[a] $\alpha \approx 4$. The primary goal of the first set of experiments is to demonstrate enhanced laser coupling in implosions with narrow-beam illumination.[25] The experiments use fixed-diameter (860-μm) nominal OMEGA targets and variable-diameter beams. The beam diameters are varied by defocusing beams obtained using small distributed phase plates (DPP's).[26] Figure 129.10 shows the measured beam profiles for different defocus offsets corresponding to different $R_{\text{beam}}/R_{\text{target}}$.

The experiments with variable beams use a range of $R_{\text{beam}}/R_{\text{target}}$ from 0.5 to 1.09. Figure 129.11 compares measured and simulated scattered-light spectra for wide and narrow beams ($R_{\text{beam}}/R_{\text{target}} = 1.0$ and 0.5, respectively). Note the good agreement between the simulated and measured spectra. The implosion with narrow beams and reduced CBET shows the presence of the red-shifted part of the spectrum, which corresponds to light that deeply penetrates inside the target corona.
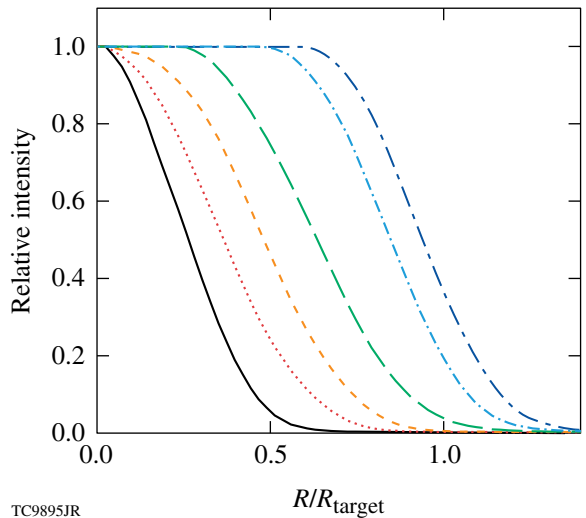

Figure 129.10
Measured profiles of beams with small distributed phase plates (DPP's) at different defocus offsets. The beam profile at best focus is shown by the solid line and wider beams have increasing defocus offsets. These profiles correspond to $R_{\text{beam}}/R_{\text{target}} = 0.5, 0.65, 0.74, 0.88, 1.0,$ and 1.09 (from narrow to wide, respectively).

_____

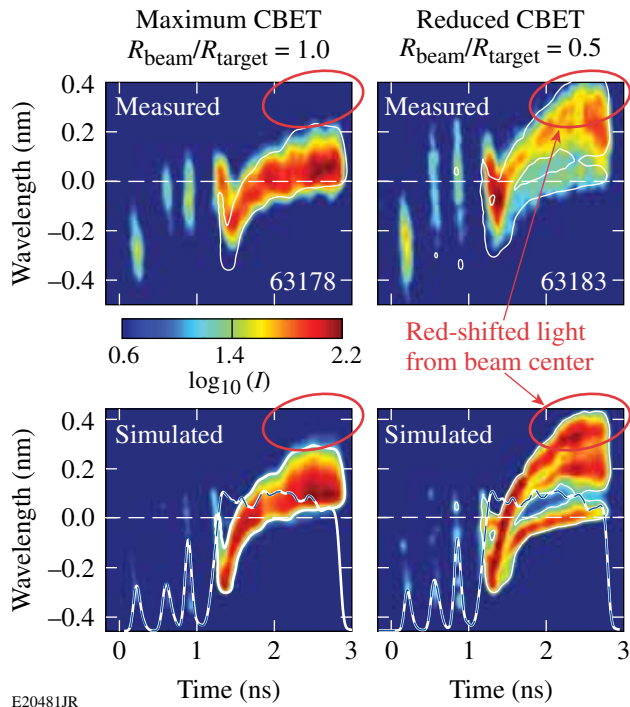[a]The ratio of the pressure in an imploding shell to the Fermi-degenerate pressure.

Figure 129.11
Measured and simulated scattered-light spectra for plastic-shell implosions using wide and narrow laser beams (R_{beam}/R_{target} =1.0 and 0.5, respectively). The implosion with narrow beams recovers the red-shifted part of the spectrum (shown by the red ovals), which corresponds to rays that deeply penetrate into the target corona. These rays are not present in the implosion with wide beams $\left(R_{beam}/R_{target} = 1.0\right)$ because of CBET. Note good agreement between measured and simulated spectra.

The implosions with wide beams $\left(R_{beam}/R_{target} = 1.0\right)$ do not show such red-shifted parts, indicating that deeply penetrated light has been scattered.

Figure 129.12 shows the scattered-light fractions in implosions with different R_{beam}/R_{target}. The measured fractions (solid red circles with error bars) are reduced in implosions with narrower beams, in agreement with simulations that include CBET (triangles and solid line). The reduction in scattered light and corresponding increase in absorption result in earlier bang times in implosions with narrow beams. Figure 129.13 summarizes the bang-time measurements and shows good agreement between the measurements (solid circles) and simulations with CBET (triangles).

The earlier bang times correspond to higher-velocity implosions in agreement with the results of the ablation-front trajectory measurements. Figure 129.14(a) shows two examples of trajectories both measured (squares) and simulated with CBET (lines), for R_{beam}/R_{target} =1.0 and 0.75. The targets illumi-
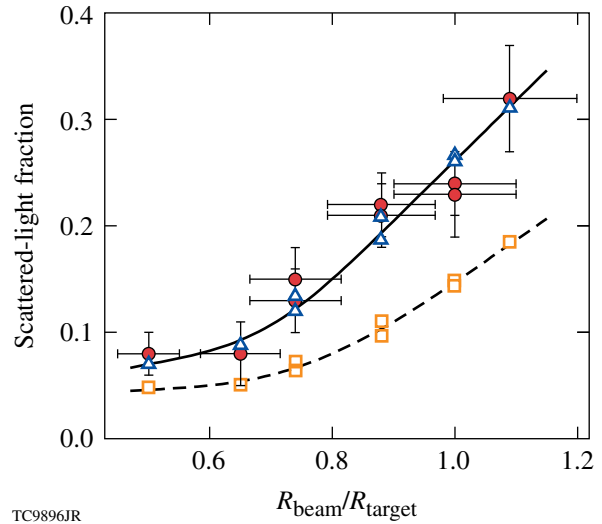

Figure 129.12
Scattered-light fractions in implosion experiments using variable-diameter beams. Measurements corresponding to implosions with different R_{beam}/R_{target} are shown by the solid red circles with error bars. Simulation results with and without CBET are shown by the blue open triangles and orange open squares and approximated by the solid and dashed lines, respectively. The measured fractions are in good agreement with the simulated ones including CBET.
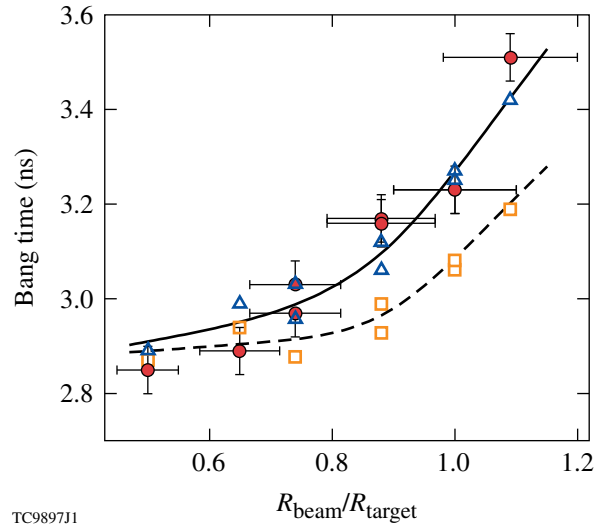

Figure 129.13
Bang times in implosion experiments using variable-diameter beams. (For notations see Fig. 129.12.) The measured bang times are in good agreement with the simulated ones including CBET.

nated with smaller beams clearly demonstrate higher velocity. Figure 129.14(b) compares the implosion velocities inferred from the measured trajectories (squares) and those simulated with and without CBET (triangle and diamonds, respectively).
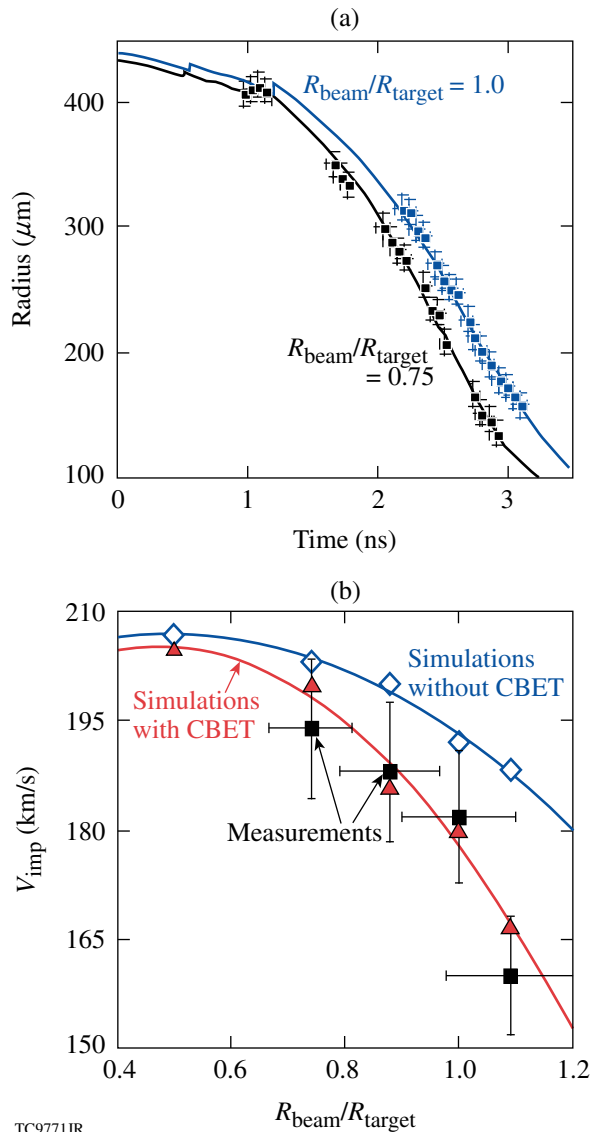
Figure 129.14

(a) Ablation-front trajectories inferred from x-ray framing camera images (squares) and simulated (lines) in implosions with wide and narrow beams ($R_{beam}/R_{target} = 1.0$ and 0.75, respectively). (b) Measured (squares) and simulated with (red line and triangles) and without (blue line and diamonds) CBET implosion velocities as functions of R_{beam}/R_{target}. Higher implosion velocities are achieved with smaller beams in both measurements and simulations.

Higher implosion velocities are achieved with smaller beams in both measurements and simulations, and the simulations with CBET show good agreement with the measured data (triangles and squares).

The described experiments cannot, however, be used to demonstrate improvements in neutron yield because of the significant level of single-beam nonuniformity (imprint) when using beams smaller than target diameters. As a result, mea-

sured neutron yields are reduced by a factor of 5 to 10 with respect to the yields in similar implosions but illuminated with best uniformity. To address the issue of yield improvement, additional experiments employing uniform beams with standard OMEGA SG4 DPP's, polarization smoothing (PS),[27] and smoothing by spectral dispersion (SSD)[28] were performed. The SG4 DPP's with PS and SSD are optimized for the on-target uniformity in the case of 860-μm-diam targets. These experiments vary R_{beam}/R_{target} by changing the target size. The three target diameters used—860, 950, and 1000 μm—correspond to $R_{beam}/R_{target} = 0.97, 0.88$, and 0.83, respectively. This range of R_{beam}/R_{target} was narrower than that used in the previous set of experiments but covers the important region around $R_{beam}/R_{target} \sim 0.8$, where significant changes in neutron yield are expected because of beam-overlap nonuniformities. To reduce the effects of small-scale single-beam imprinting, the implosions were designed to be robust to Rayleigh–Taylor instability,[29] having relatively low in-flight aspect ratio[1] IFAR ≈ 30, which was about the same for all targets.

Figure 129.15(a) shows measured neutron yields that were normalized to simulations including CBET (circles) as a function of R_{beam}/R_{target}. If all nonuniformity sources are kept constant for different R_{beam}/R_{target}, then expected measured yields normalized to predicted yields should be independent of R_{beam}/R_{target}. This is shown in Fig. 129.15(a) by the dashed line. The data follow this line down to $R_{beam}/R_{target} \approx 0.86$. For smaller R_{beam}/R_{target}, the relative yields drop because of enhanced beam-overlap nonuniformity. Figure 129.15(b) demonstrates the benefit of using narrow beams, showing the same measurements as in Fig. 129.15(a) but normalized to simulations without CBET and assuming $R_{beam}/R_{target} = 1$. Such a normalization uses "clean" yields without both beneficial effects of narrow beams: reduced CBET and more-normal light illumination. The relative yields in Fig. 129.15(b) show an increase by a factor of ~1.5 for smaller beams with the maximum yield at $R_{beam}/R_{target} \approx 0.88$. Further reduction of R_{beam}/R_{target} results in a reduction in yields, indicating that beam-overlap nonuniformities dominate the target performance. These data demonstrate the beneficial effects of reducing R_{beam}/R_{target} from ~1 down to ≈ 0.85.

2. Multicolored Lasers

The efficiency of CBET is determined by the SBS gain, which is resonant and sensitive to a wavelength separation $\Delta\lambda$ between interacting beams [see Eqs. (A2) and (B8) in Appendices A and B]. Changing the wavelengths of beams affects the SBS gain and, therefore, increases or decreases CBET. Benefits of a wavelength separation technique were recently demon-
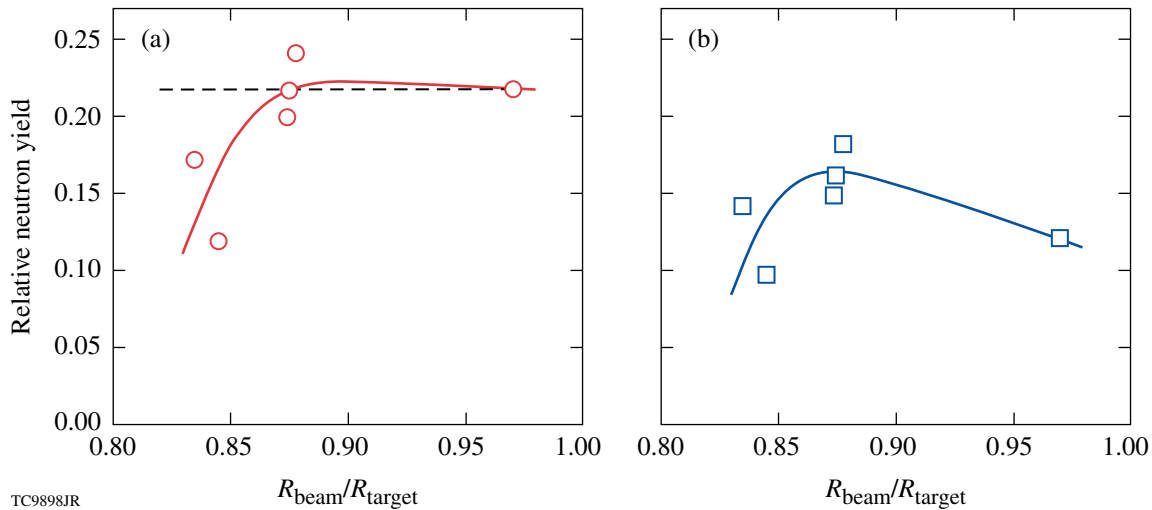
TC9898JR

Figure 129.15
Relative neutron yields in experiments using uniform beams and variable-diameter targets. (a) Measured yields normalized to simulations with CBET (circles). (b) The same yields as in (a) but normalized to simulations without CBET and having $R_{beam}/R_{target} = 1$ (squares). The solid lines in (a) and (b) approximate the data points. The dashed line in (a) shows an expected constant relative yield in the case of similar uniformity. The drop of relative yields at $R_{beam}/R_{target} < 0.86$ is due to an increase in beam-overlap nonuniformities at small R_{beam}/R_{target}.

strated in indirect-drive implosions on the NIF.[30] The applied $\Delta\lambda$ in these implosions is relatively small (up to ~3 Å in UV light). Mitigation of CBET in direct-drive implosions requires a larger $\Delta\lambda$ among beams to eliminate the coupling resonances.[13]

To illustrate the CBET mitigation effect in direct-drive experiments, consider the simplest case of a laser system operating on two subsets of lasers with wavelengths separated by $\Delta\lambda$. These wavelengths can be distributed among different beams, or each beam can include both wavelengths (e.g., as a uniform mix, or one wavelength at the center and the other at the edge of a beam). For a large separation,

$$\Delta\lambda \gg \lambda_L\left(c_a/c\right) \sim 5\,\text{Å}, \qquad (2)$$

one subset does not "see" the presence of the other and there is no interaction between them [i.e., gain length L_{ij} becomes large, see Eq. (1)]. Here, $c_a = \sqrt{(ZT_e + 3T_i)/M_i}$ is the ion-acoustic sound speed, Z is the ionization, M_i is the ion mass, and T_e and T_i are the electron and ion temperatures, respectively. In this case of large $\Delta\lambda$, CBET occurs only within each subset and, therefore, the total CBET is reduced by 1/2 with respect to the case of $\Delta\lambda = 0$. [This reduction is equivalent to assuming $\xi = 1/2$ in Eq. (1)]. Figure 129.16 shows simulated absorption fractions (solid line) for a plastic-shell implosion driven by two-color illumination as a function of $\Delta\lambda$. The absorption fraction changes very little for $\Delta\lambda < 3$ Å and increases significantly (by up to 10%) for $\Delta\lambda > 5$ Å. The dashed line in Fig. 129.16
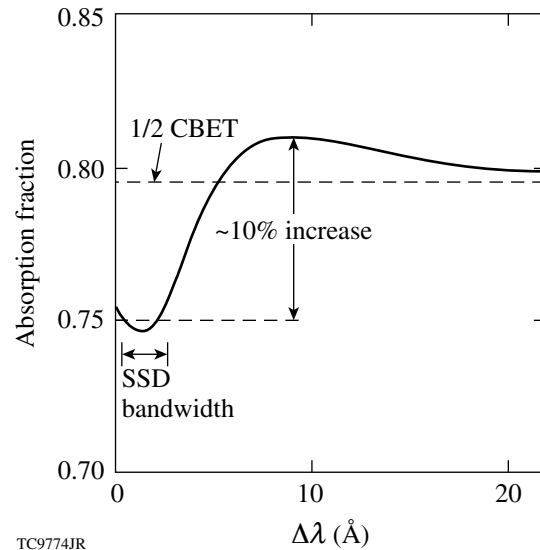
TC9774JR

Figure 129.16
Simulated absorption fraction (solid line) as a function of the wavelength separation $\Delta\lambda$ in a plastic-shell implosion using two-color light. The upper dashed line corresponds to 50%-reduced CBET using one-color light.

shows the asymptotic limit of 1/2 CBET. In general, an N-color separation can result in the asymptotic reduction of CBET by a factor of $1/N$.

As a practical application of laser drive using two or more colors distributed among different beams, a uniform spatial mix of these beams is suggested. More beams will provide a better

mixing uniformity, and using more colors is more beneficial in reducing CBET.

The results discussed in this section neglect the effects of TPD instability and laser speckles. The presence of speckles and anomalous absorption resulting from TPD can significantly modify the results shown in Fig. 129.16 that were obtained using a simple linear theory and the planar wave approximation [Eq. (1)]. Implosion experiments on OMEGA suggest that both these mechanisms, TPD and speckles, are not important at intensities $I \lesssim 6 \times 10^{14}$ W/cm^2 (see **CBET in OMEGA Implosions**, p. 3). One can expect that the multicolored technique can work in implosions within this range of intensities, and more theoretical study is required to accurately predict laser coupling at higher intensities.

3. High-Z Dopants

The dependence of CBET on plasma ion charge Z is complex (see Appendices A and B). Ion charge also affects other aspects of implosion physics: in particular, heat transport and hydrodynamics.

Figure 129.17 presents simulation results for implosion plastic shells with the varied dopant concentration of Ge: 0%, 1%, and 4%. The absorption fraction grows with increased Ge concentration in simulations both including (circles) and not including (triangles) CBET. The simulations including CBET show an ~6% larger increase in absorption for 4%-Ge
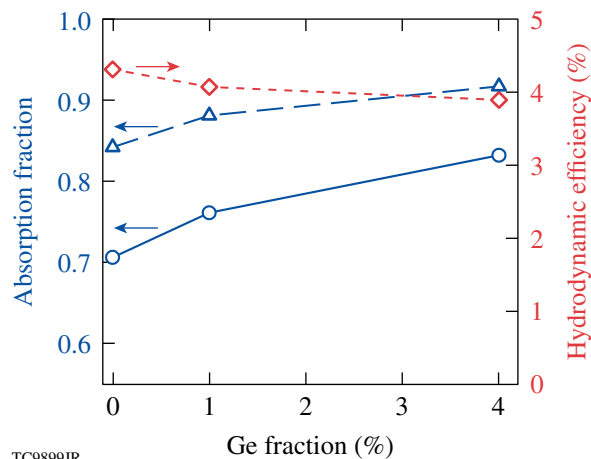
TC9899JR

Figure 129.17
Simulated absorption fractions with (solid line and circles) and without (blue dashed line and triangles) CBET for imploded plastic shells with different fractions of doped Ge. The effect of CBET is reduced in implosions with a higher-Ge dopant. Hydrodynamic efficiency in implosions with CBET (red dashed line and diamonds) is decreased with increasing-Ge dopant.

doping. These indicate a reduction of CBET in implosions with doped ablators, which is mainly caused by increased coronal electron temperature in these implosions. On the other hand, because of less-effective heat transport in a higher-Z coronal plasma, the hydrodynamic efficiency of these implosions is reduced. The simulations show that 4%-Ge dopant reduces the hydrodynamic efficiency by ~5% (see diamonds in Fig. 129.17), reducing the overall benefit of using high-Z dopants in direct-drive implosions.

Conclusions

CBET can significantly reduce the performance of direct-drive ICF implosions. It is responsible for about 10% reduction of laser absorption and about 20% reduction of hydrodynamic efficiency in implosion experiments on OMEGA. CBET is observed in time-resolved, scattered-light spectra as a suppression of red-shifted light during the main laser drive. This light is present in simulations without CBET, indicating that CBET mostly scatters the center-beam incoming light, which otherwise would penetrate to higher-density corona regions, where it is reflected with the maximum red shift.

Two models of CBET have been developed and implemented into the laser-absorption package of the 1-D hydrodynamic code *LILAC*: a fluid model (Appendix A) and a kinetic model (Appendix B), assuming spherically symmetric laser illumination of implosion targets. Both models were extensively tested using different OMEGA implosions with varied laser energies, pulse shapes, and target structure and composition. These demonstrated good agreement between model predictions and observables, which include scattered-light spectra and power, bang times, shell trajectories, and neutron yields (see **CBET in OMEGA Implosions**, p. 3). The fluid and kinetic models show quite similar results between each other.

The performance of direct-drive targets can be improved by mitigating CBET. This article considered three mitigation techniques: using narrow beams, using multicolored lasers, and high-Z–doped ablators. The first technique is efficient in improving laser coupling. The implosion experiments on OMEGA show a significant decrease of scattered-light power, earlier bang times, and an increase in implosion velocity (see Figs. 129.12–129.14) when reducing the beam radius. The small beams introduce more beam-overlap nonuniformities that reduce implosion performance by decreasing neutron yields. The experiments on OMEGA suggest an optimum $R_{\text{beam}}/R_{\text{target}} \sim 0.85$ that maximizes the performance by balancing CBET with the effects of beam-overlap nonuniformities (see Fig. 129.15).

Simulations suggest that using multicolored lasers can be another efficient technique to mitigate CBET. By splitting light into N separate colors, CBET can be reduced by a factor of ~1/N. This technique requires, however, relatively large wavelength separations $\Delta\lambda$ [Eq. (2)], which probably cannot be achieved on the OMEGA and NIF lasers. To utilize the multicolored split technique, future direct-drive laser systems should be designed to use subsets of lasers operating at different wavelengths. Such systems can benefit from using the narrow-beam technique discussed above and using many separate beams to reduce beam-overlap nonuniformity.

Test simulations of imploded plastic shells doped with high-Z elements reveal no advantages to using this technique. Unless the simulations show a relative reduction in CBET and improvement in laser coupling in the case of Ge-doped targets, the overall implosion performance suffers because of the reduction in heat transport in a higher-Z coronal plasma (see Fig. 129.17).

ACKNOWLEDGMENT

Appendix A: Fluid Equations

The fluid approach for the CBET model is based on the electron-density equation, the equation of motion for ions, and the wave equation for laser light.[8] The steady-state interaction of two light waves of the same linear polarization and an ion-acoustic wave is considered in the strong damping limit. Details of derivation of the equation for the probe-light intensity I_{probe} are given in Ref. 9; this equation can be written as

$$\frac{dI_{probe}}{d\ell} = \frac{I_{probe}}{L},\qquad(A1)$$

where ℓ is the probe-light path,

$$L^{-1} = \frac{\pi}{\lambda_L}\frac{n_e/n_{cr}}{\sqrt{1 - n_e/n_{cr}}}$$
$$\times \frac{1}{\left[\tilde{v}_a^2\eta^2 + \left(1 - \eta^2\right)^2\right]^{1/2}}\left(\frac{I_{pump}}{I_{probe}}\right)^{1/2}\left|\frac{\tilde{n}_e}{n_e}\right|\qquad(A2)$$

is the SBS spatial gain rate,

$$\left|\frac{\tilde{n}_e}{n_e}\right| = \frac{e^2\lambda_L^2}{\pi m_e^2 c^3}\frac{Z}{c_a^2}\left(\frac{m_e}{M_i}\right)\frac{\left(I_{probe}I_{pump}\right)^{1/2}}{\left[\tilde{v}_a^2\eta^2 + \left(1 - \eta^2\right)^2\right]^{1/2}}\qquad(A3)$$

is the relative amplitude of electron-density perturbations in the ion-acoustic wave, and I_{pump} is the pump-light intensity. In Eqs. (A2) and (A3), $\tilde{v}_a = v_a/k_a c_a$ is the dimensionless damping of ion-acoustic waves.[31] The variable η includes the dependency on geometry and frequency of the interacting waves,

$$\eta = \frac{(\mathbf{k}_a \cdot \mathbf{u})}{k_a c_a} - \frac{\omega_a}{k_a c_a},\qquad(A4)$$

where $\mathbf{u}$ is the flow velocity and ω_a and $\mathbf{k}_a$ are the ion-acoustic wave frequency and wave vector, respectively. The interacting waves satisfy the following three-wave matching conditions:

$$\omega_a = \omega_{probe} - \omega_{pump}\qquad(A5)$$

and

$$\mathbf{k}_a = \mathbf{k}_{probe} - \mathbf{k}_{pump}.\qquad(A6)$$

The frequency changes in probe and pump light are calculated considering the plasma expansion and Doppler effects.[32] More details of implementation of Eq. (A1) into *LILAC* can be found in Ref. 13.

Appendix B: Kinetic Equations

The electron-density perturbation $\tilde{n}_e$ in an ion-acoustic wave is calculated using the linearized Vlasov equations for electrons and ions and the Poisson equation for the self-consistent electrostatic potential. One gets[33]

$$\tilde{n}_e = \frac{k_a^2\phi_p}{4\pi e}\frac{\chi_e\left(1 + \Sigma_i\chi_i\right)}{1 + \chi_e + \Sigma_i\chi_i},\qquad(B1)$$

where the summation is taken over all ion species, ϕ_p is the beat ponderomotive potential of interacting light waves, χ_e and χ_i are the electron and ion linear susceptibilities, respectively, which can be written as follows:

$$\chi_e \approx \omega_{pe}^2/k_a^2 v_{T_e}^2,\qquad(B2)$$

$$\chi_i = \frac{\omega_{pi}^2}{k_a^2 v_{T_i}^2}\left(1 + \frac{x}{\sqrt{\pi}}\int_{-\infty}^{\infty}\frac{e^{-z^2}}{z - x}dz\right), \qquad \text{(B3)}$$

and

$$x = \frac{\omega_a + i\nu_{ie} - (\mathbf{k}_a \cdot \mathbf{u})}{\sqrt{2}\, k_a v_{T_i}}. \qquad \text{(B4)}$$

In the above equations, $v_{T_e} = (T_e/m_e)^{1/2}$ and $v_{T_i} = (T_i/M_i)^{1/2}$ are the electron and ion thermal velocities, respectively; ν_{ie} is the ion–electron collisional frequency; and $\omega_{pe} = (4\pi e^2 n_e/m_e)^{1/2}$ and $\omega_{pi} = (4\pi e^2 Z n_e/M_i)^{1/2}$ are the electron and ion plasma frequencies, respectively.

The equation for light waves is

$$\frac{\partial^2 \mathbf{A}}{\partial t^2} - c^2 \Delta \mathbf{A} + \omega_{pe}^2\left(1 + \frac{\tilde{n}_e}{n_e}\right)\mathbf{A} = 0. \qquad \text{(B5)}$$

Assuming that the probe and pump waves are *s*-polarized, the corresponding component of the vector potential $\mathbf{A}$ can be expressed as

$$A(\mathbf{r},t) = \frac{1}{2}\Big[A_{probe}\exp\left(-i\omega_{probe}t + i\mathbf{k}_{probe}\mathbf{r}\right)$$

$$+ A_{pump}\exp\left(-i\omega_{probe}t + i\mathbf{k}_{probe}\mathbf{r}\right) + \text{c.c.}\Big]. \qquad \text{(B6)}$$

Then the potential ϕ_p takes the form

$$\phi_p = -\frac{e}{2m_e c^2}A_{probe}A_{pump}^*. \qquad \text{(B7)}$$

Substituting Eq. (B1) into Eq. (B5), and using Eqs. (B6) and (B7), and the definition $A^2 = 8\pi cI/\omega_L^2$, where ω_L in the laser frequency, one obtains the equation for the probe light-intensity I_{probe}, similar in form to Eq. (A1), in which

$$L^{-1} = \frac{\pi}{\lambda_L}\frac{n_e/n_{cr}}{\sqrt{1 - n_e/n_{cr}}}\frac{\mathrm{Im}(B)}{|B|}\left(\frac{I_{pump}}{I_{probe}}\right)^{1/2}\left|\frac{\tilde{n}_e}{n_e}\right|, \quad \text{(B8)}$$

$$\left|\frac{\tilde{n}_e}{n_e}\right| = \frac{e^2\lambda_L^2}{\pi m_e^2 c^3}\frac{k_a^2}{\omega_{pe}^2}\frac{(I_{probe}I_{pump})^{1/2}}{|B|}, \qquad \text{(B9)}$$

and

$$B = \frac{1 + \chi_e + \Sigma_i\chi_i}{\chi_e(1 + \chi_i)}. \qquad \text{(B10)}$$

The interacting ion-acoustic and light waves satisfy the matching conditions given by Eqs. (A5) and (A6). Equations (B8) and (B9) substitute the fluid approach equations [Eqs. (A2) and (A3)] in the numerical procedure when the kinetic option is chosen.

Appendix C: The Clamp Model

The amplitude of ion-acoustic waves can experience a nonlinear saturation, depending on the laser intensities and ion composition of a plasma. This saturation can reduce an energy transfer predicted by the CBET model. A simple model for clamping of ion-acoustic waves was proposed[16] that limits the amplitude of electron-density perturbations $\left|\tilde{n}_e/n_e\right|$ defined by Eqs. (A3) and (B9) for the fluid and kinetic models, respectively. Specifically, the corresponding values of $\left|\tilde{n}_e/n_e\right|$ in Eqs. (A2) and (B8) are substituted by

$$\left\langle\frac{\tilde{n}_e}{n_e}\right\rangle = \min\left[\left|\frac{\tilde{n}_e}{n_e}\right|, \left(\frac{\tilde{n}_e}{n_e}\right)_{cl}\right]. \qquad \text{(C1)}$$

The clamping parameter $\left(\tilde{n}_e/n_e\right)_{cl}$ is determined from experiments.

REFERENCES

1. J. D. Lindl, *Inertial Confinement Fusion: The Quest for Ignition and Energy Gain Using Indirect Drive* (Springer-Verlag, New York, 1998). pp. 39 and 61.

2. R. L. McCrory, D. D. Meyerhofer, R. Betti, R. S. Craxton, J. A. Delettrez, D. H. Edgell, V. Yu Glebov, V. N. Goncharov, D. R. Harding, D. W. Jacobs-Perkins, J. P. Knauer, F. J. Marshall, P. W. McKenty, P. B. Radha, S. P. Regan, T. C. Sangster, W. Seka, R. W. Short, S. Skupsky, V. A. Smalyuk, J. M. Soures, C. Stoeckl, B. Yaakobi, D. Shvarts, J. A. Frenje, C. K. Li, R. D. Petrasso, and F. H. Séguin, Phys. Plasmas **15**, 055503 (2008).

3. V. N. Goncharov, T. C. Sangster, T. R. Boehly, S. X. Hu, I. V. Igumenshchev, F. J. Marshall, R. L. McCrory, D. D. Meyerhofer, P. B. Radha, W. Seka, S. Skupsky, C. Stoeckl, D. T. Casey, J. A. Frenje, and R. D. Petrasso, Phys. Rev. Lett. **104**, 165001 (2010).

4. S. Atzeni and J. Meyer-ter-Vehn, *The Physics of Inertial Fusion: Beam Plasma Interaction, Hydrodynamics, Hot Dense Matter*, International Series of Monographs on Physics (Clarendon Press, Oxford, 2004), p. 4750.

5. J. Paisner *et al.*, Laser Focus World **30**, 75 (1994).

6. T. R. Boehly, D. L. Brown, R. S. Craxton, R. L. Keck, J. P. Knauer, J. H. Kelly, T. J. Kessler, S. A. Kumpan, S. J. Loucks, S. A. Letzring, F. J. Marshall, R. L. McCrory, S. F. B. Morse, W. Seka, J. M. Soures, and C. P. Verdon, Opt. Commun. **133**, 495 (1997).

7. S. Skupsky, J. A. Marozas, R. S. Craxton, R. Betti, T. J. B. Collins, J. A. Delettrez, V. N. Goncharov, P. W. McKenty, P. B. Radha, T. R. Boehly, J. P. Knauer, F. J. Marshall, D. R. Harding, J. D. Kilkenny, D. D. Meyerhofer, T. C. Sangster, and R. L. McCrory, Phys. Plasmas **11**, 2763 (2004).

8. W. L. Kruer, *The Physics of Laser-Plasma Interactions*, Frontiers in Physics, Vol. 73, edited by D. Pines (Addison-Wesley, Redwood City, CA, 1988), pp. 46 and 88.

9. C. J. Randall, J. R. Albritton, and J. J. Thomson, Phys. Fluids **24**, 1474 (1981).

10. R. C. Malone, R. L. McCrory, and R. L. Morse, Phys. Rev. Lett. **34**, 721 (1975).

11. V. N. Goncharov, T. C. Sangster, P. B. Radha, R. Betti, T. R. Boehly, T. J. B. Collins, R. S. Craxton, J. A. Delettrez, R. Epstein, V. Yu. Glebov, S. X. Hu, I. V. Igumenshchev, J. P. Knauer, S. J. Loucks, J. A. Marozas, F. J. Marshall, R. L. McCrory, P. W. McKenty, D. D. Meyerhofer, S. P. Regan, W. Seka, S. Skupsky, V. A. Smalyuk, J. M. Soures, C. Stoeckl, D. Shvarts, J. A. Frenje, R. D. Petrasso, C. K. Li, F. Séguin, W. Manheimer, and D. G. Colombant, Phys. Plasmas **15**, 056310 (2008).

12. W. Seka, D. H. Edgell, J. P. Knauer, J. F. Myatt, A. V. Maximov, R. W. Short, T. C. Sangster, C. Stoeckl, R. E. Bahr, R. S. Craxton, J. A. Delettrez, V. N. Goncharov, I. V. Igumenshchev, and D. Shvarts, Phys. Plasmas **15**, 056312 (2008).

13. I. V. Igumenshchev, D. H. Edgell, V. N. Goncharov, J. A. Delettrez, A. V. Maximov, J. F. Myatt, W. Seka, A. Shvydky, S. Skupsky, and C. Stoeckl, Phys. Plasmas **17**, 122708 (2010).

14. J. Myatt, A. V. Maximov, W. Seka, R. S. Craxton, and R. W. Short, Phys. Plasmas **11**, 3394 (2004).

15. J. Delettrez, R. Epstein, M. C. Richardson, P. A. Jaanimagi, and B. L. Henke, Phys. Rev. A **36**, 3926 (1987).

16. P. Michel *et al.*, Phys. Rev. Lett. **102**, 025004 (2009).

17. R. A. Lerche, D. W. Phillion, and G. L. Tietbohl, Rev. Sci. Instrum. **66**, 933 (1995).

18. D. T. Michel, C. Sorce, R. Epstein, N. Whiting, I. V. Igumenshchev, R. Jungquist, and D. H. Froula, "Shell Trajectory Measurements from Direct-Drive Experiments," submitted to Review of Scientific Instruments.

19. P. B. Radha, C. Stoeckl, V. N. Goncharov, J. A. Delettrez, D. H. Edgell, J. A. Frenje, I. V. Igumenshchev, J. P. Knauer, J. A. Marozas, R. L. McCrory, D. D. Meyerhofer, R. D. Petrasso, S. P. Regan, T. C. Sangster, W. Seka, and S. Skupsky, Phys. Plasmas **18**, 012705 (2011).

20. D. H. Edgell, W. Seka, J. A. Delettrez, R. S. Craxton, V. N. Goncharov, I. V. Igumenshchev, J. Myatt, A. V. Maximov, R. W. Short, T. C. Sangster, and R. E. Bahr, Bull. Am. Phys. Soc. **52**, 195 (2007); *ibid.* **53**, 168 (2008); *ibid.* **54**, 145 (2009).

21. W. Seka, D. H. Froula, D. H. Edgell, J. F. Myatt, R. W. Short, I. V. Igumenshchev, V. N. Goncharov, and A. V. Maximov, Bull. Am. Phys. Soc. **56**, 327 (2011).

22. V. N. Goncharov, T. C. Sangster, R. Epstein, S. X. Hu, I. V. Igumenshchev, D. H. Froula, R. L. McCrory, D. D. Meyerhofer, P. B. Radha, W. Seka, S. Skupsky, C. Stoeckl, D. T. Casey, J. A. Frenje, and R. D. Petrasso, Bull. Am. Phys. Soc. **56**, 240 (2011).

23. A. V. Maximov, J. F. Myatt, R. W. Short, I. V. Igumenshchev, D. H. Edgell, and W. Seka, Bull. Am. Phys. Soc. **56**, 328 (2011).

24. D. Keller, T. J. B. Collins, J. A. Delettrez, P. W. McKenty, P. B. Radha, B. Whitney, and G. A. Moses, Bull. Am. Phys. Soc. **44**, 37 (1999).

25. D. H. Froula, I. V. Igumenshchev, D. T. Michel, D. H. Edgell, R. Follett, V. Yu. Glebov, V. N. Goncharov, J. Kwiatkowski, F. J. Marshall, P. B. Radha, W. Seka, C. Sorce, C. Stagnitto, C. Stoeckl, and T. C. Sangster, "Increasing Hydrodynamic Efficiency by Reducing Cross-Beam Energy Transfer in Direct-Drive Implosion Experiments," submitted to Physical Review Letters.

26. Y. Lin, T. J. Kessler, and G. N. Lawrence, Opt. Lett. **20**, 764 (1995).

27. T. R. Boehly, V. A. Smalyuk, D. D. Meyerhofer, J. P. Knauer, D. K. Bradley, R. S. Craxton, M. J. Guardalben, S. Skupsky, and T. J. Kessler, J. Appl. Phys. **85**, 3444 (1999).

28. S. P. Regan, J. A. Marozas, J. H. Kelly, T. R. Boehly, W. R. Donaldson, P. A. Jaanimagi, R. L. Keck, T. J. Kessler, D. D. Meyerhofer, W. Seka, S. Skupsky, and V. A. Smalyuk, J. Opt. Soc. Am. B **17**, 1483 (2000).

29. S. Chandrasekhar, *Hydrodynamic and Hydromagnetic Stability*, International Series of Monographs on Physics (Dover Publications, New York, 1981), p. 428.

30. P. Michel *et al.*, Phys. Plasmas **17**, 056305 (2010).

31. E. A. Williams, R. L. Berger, R. P. Drake, A. M. Rubenchik, B. S. Bauer, D. D. Meyerhofer, A. C. Gaeris, and T. W. Johnston, Phys. Plasmas **2**, 129 (1995).

32. T. Dewandre, J. R. Albritton, and E. A. Williams, Phys. Fluids **24**, 528 (1981).

33. E. A. Williams, B. I. Cohen, L. Divol, M. R. Dorr, J. A. Hittinger, D. E. Hinkel, A. B. Langdon, R. K. Kirkwood, D. H. Froula, and S. H. Glenzer, Phys. Plasmas **11**, 231 (2004).